



# Comparison of mechanical properties and structure of Haynes 282 consolidated via two different powder metallurgy methods: laser powder bed fusion and hot pressing

P. Maj<sup>1</sup> · K. Bochenek<sup>2</sup> · R. Sitek<sup>1</sup> · M. Koralnik<sup>1</sup> · K. Jonak<sup>1</sup> · M. Wieczorek<sup>1</sup> · Z. Pakieła<sup>1</sup> · J. Mizera<sup>1</sup>

Received: 3 January 2023 / Revised: 25 March 2023 / Accepted: 13 April 2023  
© The Author(s) 2023

## Abstract

The development of powder metallurgy methods in recent years has caused traditional casting methods to be replaced in many industrial applications. Using such methods, it is possible to obtain parts having the required geometry after a process that saves both manufacturing costs and time. However, there are many material issues that decrease the functionality of these methods, including mechanical properties anisotropy and greater susceptibility to cracking due to chemical segregation. The main aim of the current article is to analyze these issues in depth for two powder metallurgy manufacturing processes: laser powder bed fusion (LPBF) and hot-pressing (HP) methods—selected for the experiment because they are in widespread use. Microstructure and mechanical tests were performed in the main manufacturing directions, X and Z. The results show that in both powder metallurgy methods, anisotropy was an issue, although it seems that the problem was more significant for the samples produced via LPBF SLM technique, which displayed only half the elongation in the building direction (18%) compared with the perpendicular direction (almost 38%). However, it should be noted that the fracture toughness of LPBF shows high values in the main directions, higher even than those of the HP and wrought samples. Additionally, the highest level of homogeneity even in comparison with wrought sample, was observed for the HP sintered samples with equiaxed grains with visible twin boundaries. The tensile properties, mainly strength and elongation, were the highest for HP material. Overall, from a practical standpoint, the results showed that HP sintering is the best method in terms of homogeneity based on microstructural and mechanical properties.

**Keywords** Haynes 282 nickel alloy · LPBF · HP · SEM · Static tensile test

## 1 Introduction

Powder metallurgy methods are commonly used in various industries, including automotive, tooling, aerospace, and other industries [1]. Their main advantage is that they make it possible to form all sorts of materials (even brittle ones) into real products with limited finishing [2]. Worthy of note is that these methods can be used to form complex shapes that cannot be obtained using conventional manufacturing

methods. In general, the main steps that are necessary for this group of methods are: (1) metal powder production, (2) initial shaping of the powder, and (3) consolidation into a solid component using temperature [3]. The main parameters shared by all these techniques that affect the final product are: the chemical composition of the metal powder, the size and shape of particles, consolidation energy density, and the atmosphere of the process [4].

Two different powder metallurgy manufacturing routes were applied in this study. One was direct metal laser sintering (DMLS), which belongs to the group of laser powder bed fusion methods (LPBF) [5]. DMLS is carried out in a chamber with a non-reactive atmosphere that protects the material from excessive oxidation. The powder is consolidated, layer by layer, using a high-energy laser focused by a precise optical system. The advantages of this method are the possibility of obtaining different complicated geometries not achievable by any other conventional method, and getting

✉ P. Maj  
piotr.maj@pw.edu.pl

<sup>1</sup> Faculty of Materials Science and Engineering, Warsaw University of Technology, Wołoska 141 Str, 02-507 Warsaw, Poland

<sup>2</sup> Institute of Fundamental Technological Research, Polish Academy of Sciences, Pawińskiego 5B Str, 02-106 Warsaw, Poland

them in a much shorter time, in a single process [6]. On the other hand, the main disadvantages are the high porosity and anisotropy of the final product [7]. The mechanical properties of the 3D printed material differ, depending on the orientation of the sample in relation to the building platform. An important feature of 3D printing is that the porosity of an element and can be controlled by parameters such as the atmosphere, additional heating, and the size of the powder used for printing [8]. According to the available literature, the DMLS method makes it possible to manufacture a wide range of materials, from biomaterials [9] to aerospace engine parts [10]. After 3D printing, post-processing of the print is necessary. Most common post-processes require a low-temperature stress relieving heat treatment and a basic surface treatment, such as sanding, to reduce roughness and partially sintered grains [11]. Some studies have used optional hot isostatic pressure (HIP) to decrease the porosity and anisotropy of the microstructure [12]. The final step in practical applications of LPBF processes involves machining the element to *customize* it to the required geometrical parameters and dimensional *consistency* [13]. However, there is a strong case for obtaining approximate net shapes that meet individual requirements, since this translates into financial savings [14].

The main differences between the HP and LPBF methods mainly concern features such as formability and tooling. In LPBF, there is no need for special dedicated tooling due to the precise movement of the laser that shapes the geometry, layer by layer. Melting is limited to a small area; this has benefits (a limited area of heating, which can be precisely controlled) and drawbacks (large stress gradients, strict laser requirements, and a time-consuming processing). It is worth emphasizing that, using this method, it is possible to obtain very complex geometries with a well-developed working surface [15].

Generally, the LPBF process can be optimized by changing the laser power output and the laser pathing, which corresponds closely with the energy density output on the powder bed [16]. Too little energy can lead to high porosity due to unfused laser paths or single powder particles. On the other hand, too much energy will cause overheating and additional thermal stresses, as well as an increase in porosity [17]. Other parameters that may influence the overall quality of the material are powder size and geometry [18].

An alternative method used for consolidating Haynes 282 alloys is hot pressing. In contrast to LPBF, the HP sintering method is limited to simple geometries that can be prepared by designing special forging dies. The HP is a long-term

process, where raw powder is compacted by applied uniaxial pressure and temperature, where heating of mold (in most cases made from graphite) occurs through convection. Nevertheless, HP is still suitable for producing turbine blades [19]. It has the advantage of making it possible to achieve medium-volume production for geometrically simple products with repeatable homogeneous properties. This method is more energy and time consuming, but the use of pressure and a long processing time result in a more uniform microstructure, which can yield better mechanical properties. Naturally, a long processing time can result in grain growth, for example in comparison with SPS (Spark Plasma Sintering), but there are many examples of the beneficial effects of a long processing time on mechanical properties [20].

The main goal of present work was to obtain Haynes 282, new generation nickel-based alloy [21], by two various powder metallurgy techniques to study their mechanical properties and microstructure. The chemical composition of the alloy is shown in Table 1. The alloy is mainly used in the aerospace industry due to its high mechanical properties and creep resistance, even at temperatures exceeding 700 °C. The hardening mechanism responsible for this high strength is associated with the gamma prime phase, which is often encountered in Ni-based alloys having an FCC structure [22]. According to data in the literature, the crucial parameters are size and shape, which strongly influence the properties of the material. With increase in temperature and/or exposure time at temperatures above 700 °C, growth in precipitates decreases coherence with the matrix and facilitates dislocation movements that in turn decrease the material's overall strength. Additionally, secondary carbides enhance the properties even further, strengthening the grain boundaries—especially in terms of high-temperature creep and fatigue resistance. To obtain a material having optimal properties, it is necessary to perform heat treatment, which affects the precipitates [23]. It is also worth noting that there have been numerous studies concerning hot cracking, a phenomenon often observed in the alloy in the case of more aggressive sintering process parameters [24].

There have been a lot of literature data concerning the manufacturing of Haynes 282 [25], where the most common method is casting followed by heat treatment, which leads to a uniform microstructure with clear grain boundaries [26]. Other less common manufacturing methods include hot isostatic pressing (HIP) [27], LPBF [28], and electron beam melting (EBM) [29]. In all of these studies, a solid structure was achieved with a minimal pore content. The analyses conducted in the abovementioned studies focused mainly

**Table 1** Chemical composition of Amperprint® 0233 [30]

Element	Ni	Cr	Co	Mo	Ti	Al	C	B
Content (wt.%)	Balance	19.5	10	8.5	2.1	1.5	0.05	0.005

on microstructure and mechanical properties. Guidelines for obtaining a homogeneous structure were achieved. However, in contrast, in other studies, we achieved good fracture resistance without the need for additional heating—which some authors stated as essential [24].

The main aim of the current work is to analyze how the manufacturing method affects the tensile properties, microstructure, and fracture toughness of Haynes 282 alloy through a comparative study of bulk materials manufactured via two different powder metallurgy technologies: hot pressing and selective laser melting (with a wrought alloy as reference). The premise of the article is to analyze as-manufactured materials. Moreover, there is no data on the influence of the manufacturing method on fracture toughness analysis and high-temperature tensile tests for the materials presented in this paper. This article tries to fill these gaps.

## 2 Material

The material studied in this article was powder for an AM process of powder bed fusion made from nickel superalloy Amperprint® 0233, also known as Haynes® 282®. Amperprint® 0233 is a vacuum induction melted, gas atomized, spherical powder produced under a license from Haynes International, Inc. The diameter of the particles is between 15 and 45  $\mu\text{m}$  (max 5% over and undersize). The nominal chemical composition of the material is presented in Table 1.

To verify the as-received product, studies of particle size distribution using laser scattering were performed using a Horiba LA-950, and SEM photos were taken using a Hitachi TM-1000 scanning electron microscope. The powder particles were spherical, and 90% of them were smaller in diameter than 48  $\mu\text{m}$ . In the SEM micrographs, some shape defects can be observed, but these had no negative effect on

the additive manufacturing process. The melt pools were regular in shape and size, and no inclusions were visible in the tested samples (Fig. 1).

## 3 Methodology

The initial state material was a wrought ingot after heat treatment at 1130  $^{\circ}\text{C}$  for 4 h in accordance with the guidance for wrought material.

The printed samples were manufactured using an EOS M 100 3D printer operating in the LPBF method. The machine uses an argon atmosphere to prevent oxidation and corrosion. It also has a unique dosing system which enables the use of steel blades to distribute the powder. This guarantees that each layer of powder has the same height, which gives higher accuracy in duplicating prints than rubber or brush solutions do.

To achieve the best mechanical properties, an initial optimization was performed on small  $10 \times 10 \times 10$  mm samples, from which the highest specific density was selected. The rotation between layers was set at 67 degrees, the height of each layer was 20  $\mu\text{m}$ , the distance between each scanning line was 50  $\mu\text{m}$ , and the scanning stripes had a width of 5 mm, with a 0.1 mm overlap between each stripe.

Studies were performed using different laser power setups. E (energy input at the hatch) ranged from 58 to 91  $\text{J mm}^{-3}$ . The best material properties were observed for the sample printed with  $E = 75 \text{ J mm}^{-3}$ . This parameter is used in the article. The main parameter of the optimization was the relative density of the samples which was 99.6% for the selected samples using the Archimedes method (Fig. 2a). The second optimization parameter was Vickers hardness.

For the hot pressing, a Thermal Technology LLC hot-press was used as the alternative manufacturing route. The following parameters were applied: a temperature of

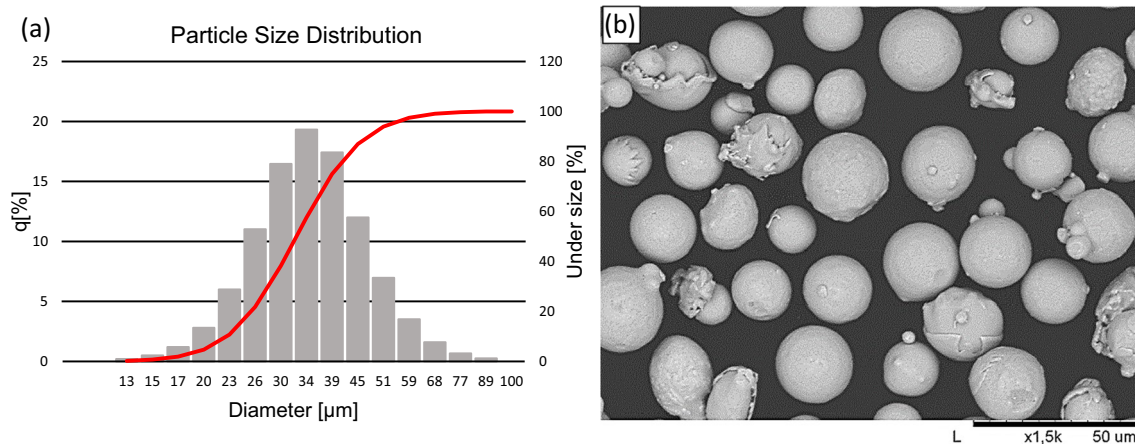
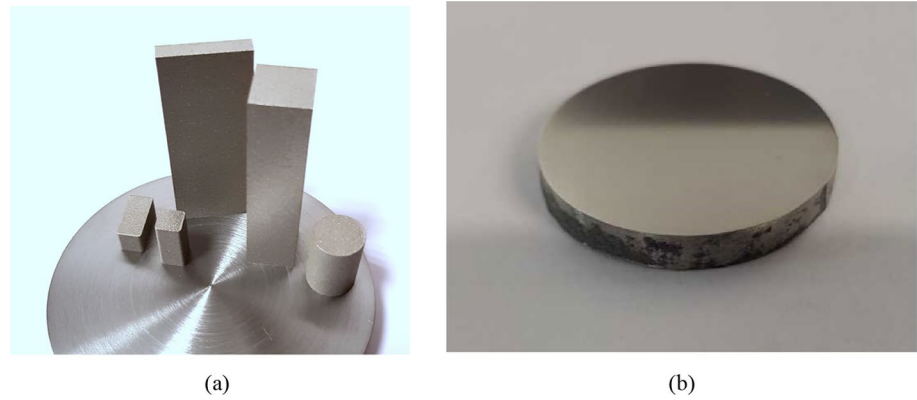


**Fig. 1** Particle size as a function of percentage of distribution (a), and SE image (b) of Amperprint® 0233 powder magnified 1.5 k times

**Fig. 2** Samples used in the experiment **a** LPBF and **b** HP sinter



1200 °C under a pressure of 30 MPa, with a heating rate of 10 °C/min, and a dwelling time of 60 min (under a vacuum). The dimensions of the compact were 48 mm in diameter and ~5 mm in height. The measured relative density of the sample was 99.8% by use of the Archimedes method (Fig. 2b).

The hardness tests were performed using a Zwick Roell 2.5 automatic hardness tester. For each sample, ten measurements were made using the Vickers method with a load of 1 kg. The distance between each measurement was longer than 2.6 times the diagonal of indentation.

Room temperature tensile tests were performed using a Zwick Z0005 Universal Testing Machine. Microsamples

with a total length of 8.6 mm were used (Fig. 3a); they had the following geometry. For each analyzed state and orientation of the material, a minimum of three tests were conducted. For LPBF, the number of samples was five, as the spread of results was much broader. High-temperature tensile tests were performed on Zwick Z050 with attached heating chamber, the geometry of samples is presented in Fig. 3b. The samples were cut using wire electro-discharge machining and then ground to achieve a relatively smooth surface without additional defects.

The tensile tests in room temperature were performed at a constant strain rate of  $10^{-3} \frac{1}{s}$ , and in accordance with previous analyses by adding digital image correlation (DIC), a technique

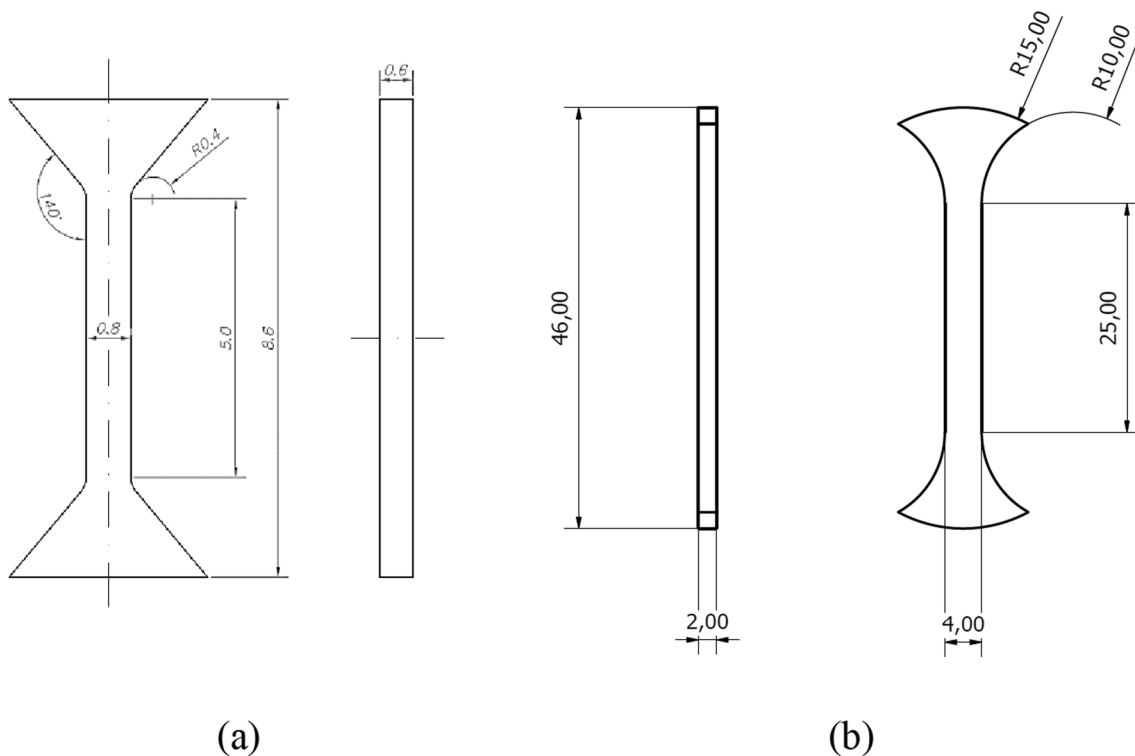


**Fig. 3** Dimensions of the microsamples used for the static tensile tests at **a** room temperature and **b** elevated temperature

that uses image analysis of individual points applied to a sample. This makes it possible to obtain reliable elongation results without the influence of measurement errors from poor fitting of the samples [31]. Additionally, in the case of the 3D printed samples, the method is very susceptible to the defects that are often encountered when using this technique [32].

The light microscopy observations were carried out using a Nikon Epiphot 200. The standard procedure of grinding, polishing, and etching was applied. Chemical etching on the Haynes 282 was performed using a solution of  $\text{HNO}_3 + \text{HCL} + \text{FeCL}$ .

The transmission electron microscope (TEM) observations were carried out using a JEOL JEM 1200EX microscope at an acceleration voltage of 120 kV. The samples were prepared using a precision ion polishing system at a beam voltage of 4 V, inclined to the sample surface at an angle of  $10^\circ$ .

The values of fracture toughness of the obtained materials were compared on a Zwick Proline Z050 universal testing machine with crosshead speed of 0.5 mm/min. Rectangular bars of  $3 \times 4 \times 25 \text{ mm}^3$  were cut from the manufactured specimens using a wire cutter (Mitsubishi MV1200R). The V-notches on the SEVNB specimens were first cut using the wire cutter and then finished using a custom-made notching machine with a razor blade and diamond paste (9/6/3/1  $\mu\text{m}$ ). Ultimately, it was possible to obtain a low-diameter notch tip (below 20 microns). The length of the notches was in a range from  $\frac{1}{4}$  up to  $\frac{1}{3}$  of the specimen's thickness.

The standard Eqs. (1) and (2) were used to calculate the fracture toughness value of the specimens:

$$K_{IC} = \frac{PS}{BW^{\frac{3}{2}}} f\left(\frac{a}{W}\right) \left[ \text{MPa}\sqrt{\text{m}} \right], \quad (1)$$

where,

$$f\left(\frac{a}{W}\right) = 3\sqrt{\frac{a}{W}} \times \frac{\left(1.99 - \frac{a}{W}\right)\left(1 - \frac{a}{W}\right)\left[2.15 - 3.93\frac{a}{W} + 2.7\left(\frac{a}{W}\right)^2\right]}{2\left(1 + 2\frac{a}{W}\right)\left(1 - \frac{a}{W}\right)^{\frac{3}{2}}}, \quad (2)$$

$P$  is the fracture load (MN),  $S$  is the support span (in case of four-point bending mode is difference between lower support span and upper support span) (m),  $B$  is the specimen width (m),  $W$  is the specimen thickness (m),  $a$  is the notch depth (m)

## 4 Results

### 4.1 Microstructure of the samples (light microscopy)

The microstructures of the Haynes 282 showed noticeable differences for the individual manufacturing methods

(Fig. 4). The grain sizes varied. In the case of the wrought material, they were equiaxed, but with size ranging from 30 to 90  $\mu\text{m}$ . The samples produced using the LPBF technique consisted of multilayers of melting pools, as is typical for 3D printed samples [25, 33]. It is worth noting that there seems to have been segregation, which is also quite typical for LPBF materials on the outskirts and in the middle of the melt pools which is visible in the differences in etching susceptibility (Fig. 3b). The most uniform structure with equiaxed grains was obtained in the HP sintered sample.

### 4.2 Transmission electron microscope

As a supplementary analysis, TEM observations were conducted for the sintered samples and those produced using the LPBF technique (Fig. 5). There were significant differences in both samples, mainly concerning the concentration of defects and the type of the grain boundaries. In the LPBF samples, much higher concentrations of dislocations can be observed. There are visible low-angle dislocation boundaries and numerous dislocation tangles inside the grains in Fig. 5d. In contrast, the HP sinter grains are devoid of dislocations, and contain visible twins—which form because of the high annealing temperature. Additionally, there are some defects at the grain boundaries, although from the electron diffractogram, only one phase is visible (Fig. 5c). Moreover, in both samples, the occurrence of small precipitates was observed in the area near the grain boundaries; these had an average size of about 30 nm.

The hardness tests showed that the highest hardness was observed in the HP sintered material, and the lowest in the wrought state, whereas the LPBF material was about 40 units lower than the HP sample. Moreover, no differences in hardness were found between the XY and XZ planes of the printed sample. It is worth noting that the sintered sample had the lowest spread of results and the wrought sample had the highest. As has been shown, the sinter sample exhibited a very uniform structure that remained unchanged throughout the volume of the material. On the other hand, the wrought material displayed a broader range of test results, mainly because of unequal grain size according to the Hall Petch strengthening equation.

The average and standard deviation in measurements are shown in Table 2.

The tensile tests were done in the main parallel and longitudinal directions (Fig. 6). It can be clearly seen that this had an impact on the LPBF and HP sintered samples—in contrast to the wrought material, in which sample orientation had almost no effect. The effect was most significant in the LPBF manufactured material. In the building direction, the elongation was almost two times lower than in the parallel direction. Strength shows a reverse relation in which the strength is 100 Mpa higher in the longitudinal direction.

**Fig. 4** Microstructure of samples Haynes 282 nickel alloy: from annealed bar (a), manufactured by LPBF printing (b) and from HP sintering (c) technique (light microscope)

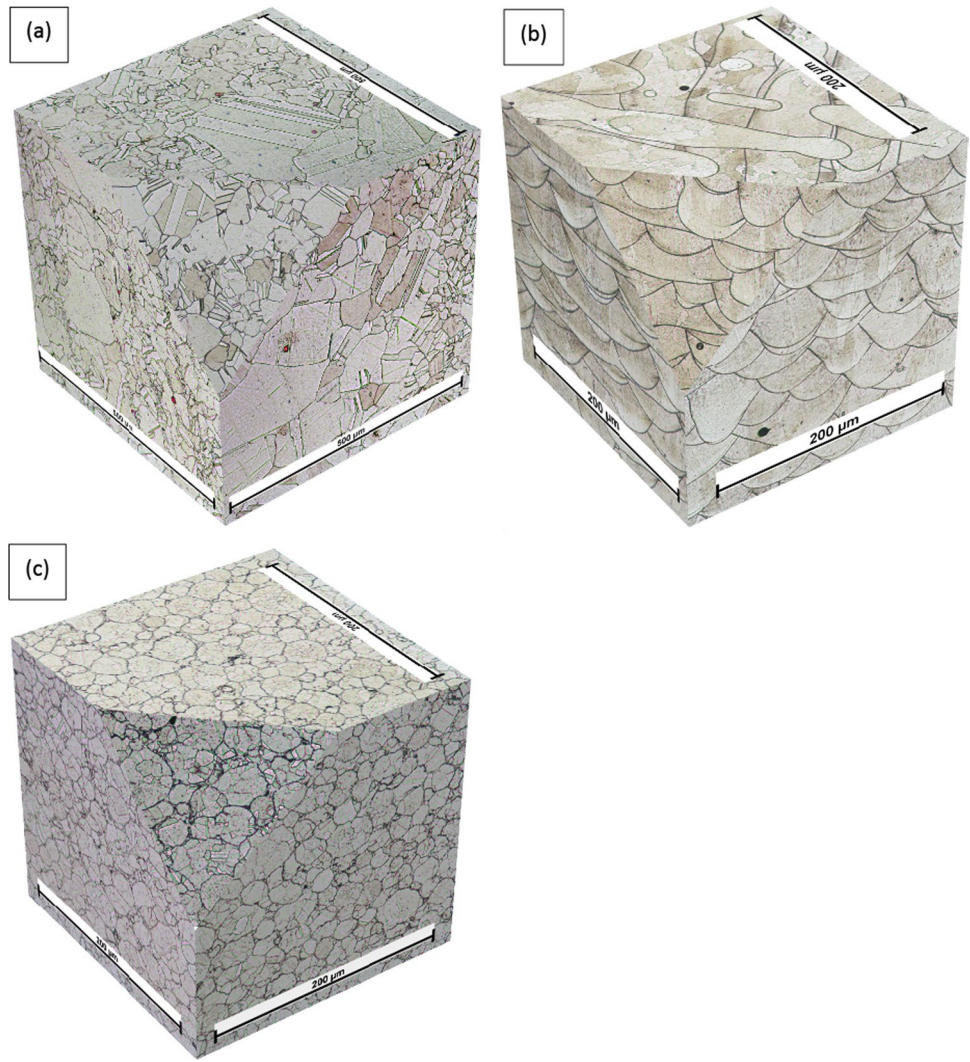


**Fig. 5** Microstructure of samples Haynes 282 produced: HP (a) and LPBF (b)

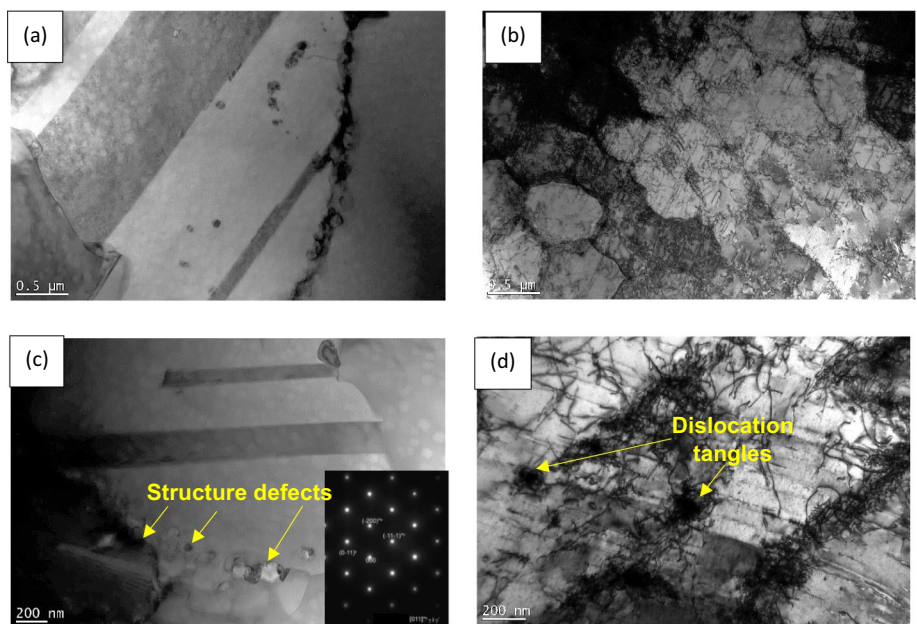


**Table 2** Results of testing hardness using the Vickers method

Material	Hardness HV1	Standard deviation
Wrought	231	11
LPBF XY	315	5
LPBF XZ	316	5
HP sintered	355	2

The slight difference between the  $R_{0.2}$  and  $R_m$  values for the LPBF sample compared with the other states is related to the material’s lower strengthening ability, which in turn is due to the large number of dislocations (confirmed by the TEM observations). In the case of the HP sintered along the pressure direction, the strength was lower along with elongation, which was most probably a result of non-uniform squeeze (probably due to the presence of twin boundaries). Overall, the highest strength and elongation were observed for the HP sintered material, as is a result of two factors: the small uniform grain size without any apparent stress concentration, and the slower cooling rate, which probably led to small sub-micro-sized precipitation that increased the material’s strength (Table 3).

In the tensile tests conducted at 750 °C, the HP sintered sample displayed the highest UTS, although its yield strength was slightly lower (Fig. 6). Additionally, the LPBF displayed very fast necking and a decrease in strength, an undesirable feature that indicates a rapid localization of deformation. In Table 4, the samples are additionally compared with data provided by the manufacturer for the annealed and age-hardened states. What stands out is the HP material, which has supreme strength and elongation comparable to the age-hardenable sheet, with a very low spread of results. All the specimens for testing were cut along the XY direction.

**Table 3** Summary of tensile test results

Sample	Direction	$R_{0.2}$ (MPa)	UTS (MPa)	A (%)
Wrought	XY	502	905	39
	XZ	510	901	37
HP sintered	XY	840	1206	24
	XZ	825	1272	31
LPBF	XY	645	872	19
	XZ	707	954	36

$R_{0.2}$  yield strength (MPa), UTS ultimate strength (MPa), A elongation (%)

**Table 4** Tensile results for Haynes 282 at 750 °C

Sample	UTS (MPa)	$R_{0.2}$ (MPa)	A (%)
HP Sinter	962 ± 7	668 ± 6	25 ± 1
LPBF	874 ± 15	783 ± 20	27 ± 3
Age-hardened sheet*	856	628	22

\*Specification sheet from manufacturer

### 4.3 Fracture toughness results

The results are presented in three- and four-point bending mode (Table 5). The three-point bending mode was performed on the wrought material due to the fact that its high plasticity results in a compression of the specimens between the lower and upper supports during testing in the four-point bending mode. Also, it well known that, for this type of material, a CT (compact tension) test will give more accurate results, but due to the limited volume of material, it was decided to perform tests in SEVNB samples. In the present paper, we focused on comparing the properties resulting from different manufacturing techniques. It is worth noting that the best results were observed for the LPBF samples,

**Fig. 6** Tensile tests curves for the three materials tested in the two main directions

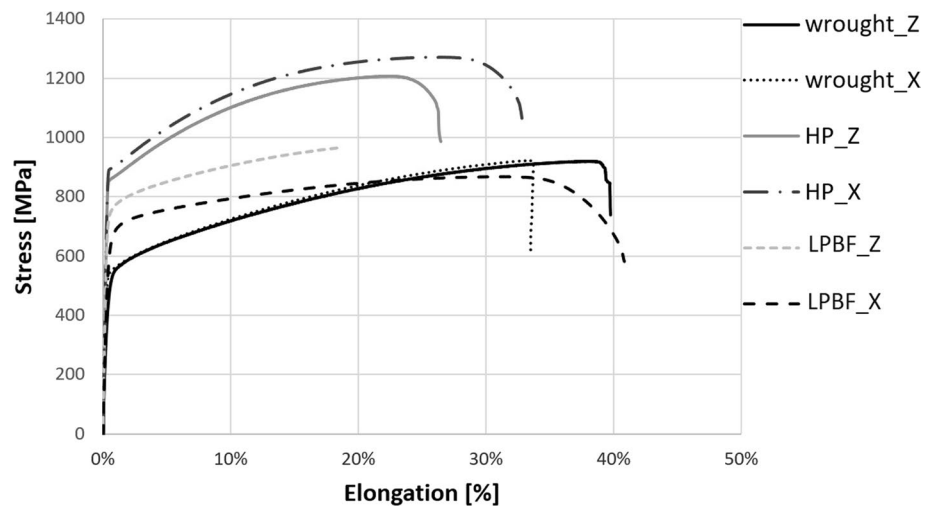


**Table 5** Fracture toughness of manufactured materials

Material	$K_{IC}$ [MPa $\sqrt{m}$ ]
Wrought	$51.95 \pm 5.0$
LPBF X	$82.5 \pm 15.2$
HP sintered X	$60.23 \pm 10.1$

which contradicts some of the results of the previous tensile tests.

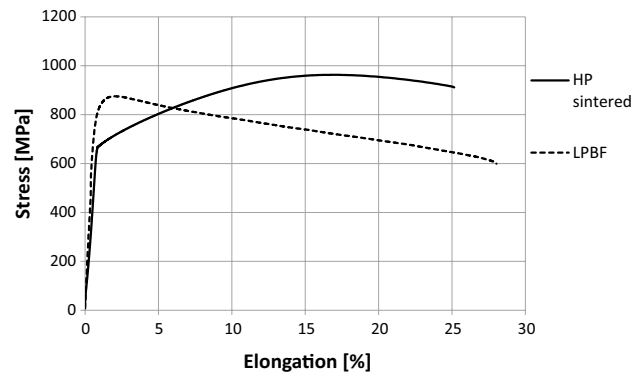
The high spread of results suggests that the key role is played by individual microstructural features, which may vary between samples. It is also worth noting that the orientation of the samples was in the *XY* plane, which reduced the impact of the layered structure typical for the LPBF technique. Additionally, the numerous grain boundaries created good conditions for energy dissipation through the creation of new crack surfaces and additional yielding around the crack fronts.

#### 4.4 Fracture analysis

Complementary to the fracture toughness analysis, fractures (Fig. 7) were analyzed by means of macro- and micro-features. Both the HP sintered and the LPBF samples showed very similar features, so only one is included in this article. The biggest changes were observed in the wrought material, which displayed higher ductility and necking. However, in both cases, tear ridges and plastic dimples were visible, although in the wrought sample, they were much bigger, most probably due to differences in grain size. Nonetheless, in all cases, ductile fracture was dominant (Fig. 8).

### 5 Discussion

The results obtained show that the manufacturing method plays a key role in determining the mechanical properties of Haynes 282. It should be noted that, overall, the alloy displays relatively high ductility and strength. This is primarily due to the solution and  $\gamma'$  strengthening [33], and is also confirmed by the current research. Nonetheless, there are also other factors that affected our results. The mechanical and structural anisotropy observed in the LPBF is a significant disadvantage compared with the other two analyzed methods. Furthermore, the literature data clearly shows that, even after an appropriate annealing process, there are differences between the wrought material and the LPBF material, especially in the building direction *Z* [25]. It has been reported that this issue mainly concerns the segregation of precipitates, structure recovery, and partial recrystallization, which prevent the material from being fully homogenous in the microregions [34]. The best composition of mechanical properties was obtained for the HP sintered sample,

**Fig. 7** Tensile results for Haynes 282 HP sintered and LPBF at 750 °C

which displayed the most homogeneous structure, as well as a moderate concentration of twins—beneficial in terms of mechanical strength [35]. Additionally, the cooling rate parameters allowed for partial strengthening with the gamma prime phase, which nucleates relatively fast in the intermediate temperature range of 800–900 °C [36]. Lastly, the grain boundaries in all the cases studied were sites of intense diffusion, as was visible in the form of the high dislocation density and precipitate concentration. It seems that, in this regard, the sample produced by the LPBF technique stands out from the other samples; this has implications regarding the mechanical properties [24] (Table 6).

Analyzing the fracture toughness results, it should be noted that all the samples displayed very high values at room temperature, which is consistent with the tensile results. In all the manufactured specimens, a crack was generated at the notch tip during loading, but this did not lead to unstable crack growth. The maximum force measured during the SEVNB test was then used in the calculations. After the generation of a crack, the recorded force dropped slightly, and the test was stopped. High values were also observed in the sample produced by the LPBF technique, in all directions, which shows that the material can maintain those values throughout the volume, regardless of orientation. Nevertheless, it seems that the sample cut in the building direction was most susceptible to cracking, probably due to its specific grain orientation, which facilitates the growth of cracks in certain directions [42]. In the fracture toughness measurements, the 3D printed Haynes 282 specimens showed the highest values, but the high deviation between the different printing directions could be a disadvantage in industrial applications.

The mechanical tests and microstructure showed that Haynes 282 has good formability by PM manufacturing, although the homogeneity of the material is an issue. The HP sintered samples seemed to be the most promising for meeting the criteria of practical applications. This includes

**Fig. 8** Fractography of the fracture toughness samples: LPBF (a, c), and wrought material (b, d)

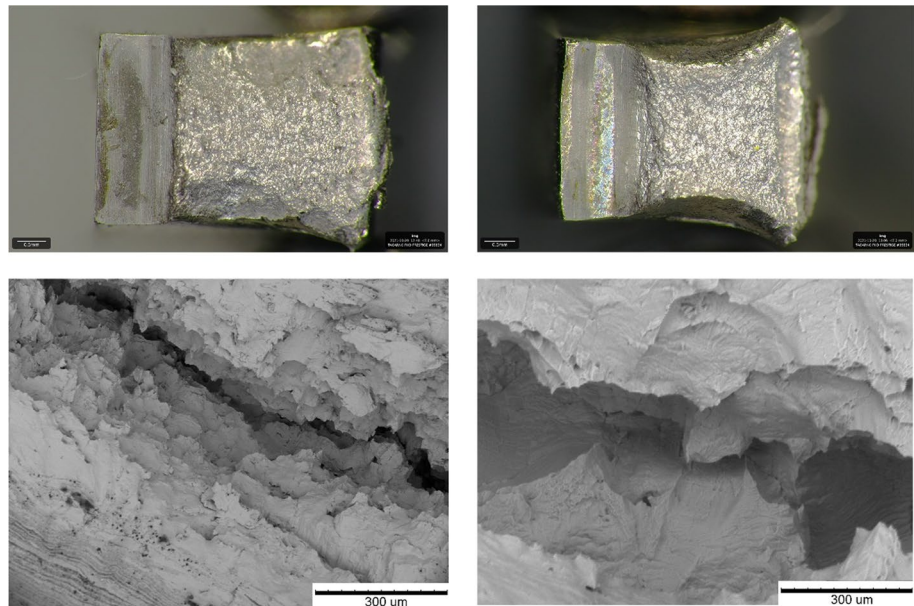


**Table 6** Summary and comparison of current results

Characteristics	Direction	Yield strength (MPa)	Ultimate yield strength (MPa)	Elongation (%)	Hardness HV	KQ	Microstructure	Reference
Solution annealed plate		404	868	60	205		Visible annealing twins and carbide $M_{23}C_6$ precipitates inside grains, Varying grain sizes	[37]
EBM printed	XY	620	1058	49			Visible carbides on GB	[38]
	XZ	656	1100	48				
LPBF printed	XZ	647	910	69			Visible Mo-rich $M_6C$ carbides	[39]
Solution annealed bar		348	816	62	171 (86Rb)		Visible melt tracks and grain boundaries stacked in layers	[40]
LPBF printed	XY	722	1012	32.4				[41]
	XZ	608	885	38.5			Uniform grain sizes	This work
	Sintered	XY	840	1206				
Solution annealed bar (wrought)	XY	502	905	39	231	52	Varying grain size, visible annealing twins and carbide precipitate directions	
	XZ	510	901	37				
LPBF printed	XY	645	872	19	315	75	Visible individual melt tracks stacked in layers	
	XZ	707	954	36				

homogeneity throughout the whole volume without any stress concentrators or visible defects. Additionally, the narrow range of grain sizes could be beneficial in terms of residual stress, which was also an issue for the wrought material. On the other hand, the LPBF Haynes displayed

large differences between the X and Z directions. This greatly reduces its potential applicability, as there would be a need for advanced machining and treatment to obtain a homogeneous material.

## 6 Conclusion

Based on the performed studies, the following conclusions can be drawn:

1. A key factor when designing a material's structure and mechanical properties is the manufacturing technology. HP stood out because of the uniform structure achieved throughout the volume of the material, which in certain respect was superior to the wrought material. The samples had negligible porosity, which is also an important feature. The LPBF material displayed very little porosity and a very fine crystalline structure with a high concentration of defects.
2. The mechanical tests showed higher strength (up to 1200 MPa) and comparable elongation in the HP samples. This was most probably related to the material's very uniform and fine microstructure, additionally enhanced by the precipitation process that took place spontaneously during cooling.
3. The high-temperature tests showed that the HP material had superior strength, even in comparison with the standard age-hardenable alloy. The disadvantages of hot-pressing technique in practice are the specialized tooling required, and that formability is limited to low-complexity geometries. The LPBF samples displayed higher yield strength, although a rapid localization of deformation was observed, which should result in significantly reduced fatigue resistance.
4. The mechanical properties of the sintered material surpassed the wrought material in relation to the manufacturer specification. This creates opportunities in enhancing high temperature properties which are of key importance for nickel-based superalloys. Based on the current results, it seems that equiaxed grains are beneficial compared to uneven recrystallized grains where the distribution is uneven. The current research can be the basis for an analysis of these phenomena, in particular in terms of the mechanical properties of aircraft alloys.

**Acknowledgements** This research was funded by POB Technologie Materiałowe of Warsaw University of Technology within the Excellence Initiative: Research University (IDUB) programme.

**Funding** This work was supported by Politechnika Warszawska.

**Data availability** All available data is available after consulting with the authors of the article.

## Declarations

**Conflict of interest** All the authors declare that there is no conflict of interest.

**Human and animal rights statement** No animal or human subjects/participants were involved in the creation of the article.

**Open Access** This article is licensed under a Creative Commons Attribution 4.0 International License, which permits use, sharing, adaptation, distribution and reproduction in any medium or format, as long as you give appropriate credit to the original author(s) and the source, provide a link to the Creative Commons licence, and indicate if changes were made. The images or other third party material in this article are included in the article's Creative Commons licence, unless indicated otherwise in a credit line to the material. If material is not included in the article's Creative Commons licence and your intended use is not permitted by statutory regulation or exceeds the permitted use, you will need to obtain permission directly from the copyright holder. To view a copy of this licence, visit <http://creativecommons.org/licenses/by/4.0/>.

## References

1. Akhtar S, Saad M, Misbah MR, Sati MC. Recent advancements in powder metallurgy: a review. *Mater Today Proc.* 2018;5(9):18649–55. <https://doi.org/10.1016/j.matpr.2018.06.210>.
2. Childerhouse T, Jackson M. Near net shape manufacture of titanium alloy components from powder and wire: a review of state-of-the-art process routes. *Metals (Basel)*. 2019. <https://doi.org/10.3390/met9060689>.
3. Delavari M, Salarvand A, Rahi A, Shahri F. The effect of powder metallurgy process parameters on mechanical properties of micro and nano-iron powder. *Int J Eng Sci Technol.* 1970;3(9):86–94. <https://doi.org/10.4314/ijest.v3i9.7>.
4. Sudha GT, Stalin B, Ravichandran M. Optimization of powder metallurgy parameters to obtain low corrosion rate and high compressive strength in Al-MoO<sub>3</sub> composites using SN ratio and ANOVA analysis. *Mater Res Express.* 2019. <https://doi.org/10.1088/2053-1591/ab2cef>.
5. Leary M. Powder bed fusion. In: *Design for additive manufacturing*. Elsevier; 2020. pp. 295–319. <https://doi.org/10.1016/B978-0-12-816721-2.00011-7>.
6. Kumar S. Selective laser sintering/melting. In: *Comprehensive materials processing*. Elsevier; 2014. pp. 93–134. <https://doi.org/10.1016/B978-0-08-096532-1.01003-7>.
7. Gokuldoss PK, Kolla S, Eckert J. Additive manufacturing processes: selective laser melting, electron beam melting and binder jetting—selection guidelines. *Materials.* 2017;10(6):672. <https://doi.org/10.3390/ma10060672>.
8. Wysocki B, et al. Microstructure and mechanical properties investigation of CP titanium processed by selective laser melting (SLM). *J Mater Process Technol.* 2017. <https://doi.org/10.1016/j.jmatprotec.2016.10.022>.
9. Chmielewska A, Jahadabkar A, Wysocki B, Elahinia M, Świączkowski W, Dean D. Chemical polishing of additively manufactured, porous, Nickel–Titanium skeletal fixation plates. *3D Print Addit Manuf.* 2021. <https://doi.org/10.1089/3dp.2020.0209>.
10. Seabra M, et al. Selective laser melting (SLM) and topology optimization for lighter aerospace components. *Procedia Struct Integr.* 2016;1:289–96. <https://doi.org/10.1016/j.prostr.2016.02.039>.
11. Boschetto A, Bottini L, Macera L, Veniali F. Post-processing of complex SLM parts by barrel finishing. *Appl Sci (Switz)*. 2020. <https://doi.org/10.3390/app10041382>.
12. Liu S, Guo H. Influence of hot isostatic pressing (HIP) on mechanical properties of magnesium alloy produced by selective laser

- melting (SLM). *Mater Lett.* 2020;265:127463. <https://doi.org/10.1016/j.matlet.2020.127463>.
13. Hintze W, von Wenserski R, Junghans S, Möller C. Finish machining of Ti6Al4V SLM components under consideration of thin walls and support structure removal. *Procedia Manuf.* 2020;48:485–91. <https://doi.org/10.1016/j.promfg.2020.05.072>.
  14. Riveiro A, et al. Laser additive manufacturing processes for near net shape components. 2019. [https://doi.org/10.1007/978-3-030-10579-2\\_5](https://doi.org/10.1007/978-3-030-10579-2_5).
  15. Druzgalski CL, Ashby A, Guss G, King WE, Roehling TT, Matthews MJ. Process optimization of complex geometries using feed forward control for laser powder bed fusion additive manufacturing. *Addit Manuf.* 2020. <https://doi.org/10.1016/j.addma.2020.101169>.
  16. Kladovasilakis N, Charalampous P, Tsongas K, Kostavelis I, Tzovaras D, Tzetzis D. Influence of selective laser melting additive manufacturing parameters in Inconel 718 Superalloy. *Materials.* 2022;15(4):1–19. <https://doi.org/10.3390/ma15041362>.
  17. Yang Y, van Keulen F, Ayas C. A computationally efficient thermal model for selective laser melting. *Addit Manuf.* 2020;31(July 2019):100955. <https://doi.org/10.1016/j.addma.2019.100955>.
  18. Zhang J, et al. Influence of particle size on laser absorption and scanning track formation mechanisms of pure Tungsten powder during selective laser melting. *Engineering.* 2019;5(4):736–45. <https://doi.org/10.1016/j.eng.2019.07.003>.
  19. Voisin T, Monchoux JP, Durand L, Karnatak N, Thomas M, Couret A. An innovative way to produce  $\gamma$ -TiAl blades: spark plasma sintering. *Adv Eng Mater.* 2015;17:1408–13. <https://doi.org/10.1002/adem.201500019>.
  20. Bochenek K, Węglewski W, Morgiel J, Basista M. Influence of rhenium addition on microstructure, mechanical properties and oxidation resistance of NiAl obtained by powder metallurgy. *Mater Sci Eng A.* 2018;735:121–30. <https://doi.org/10.1016/j.msea.2018.08.032>.
  21. Haynes® International Inc. Haynes®282®Alloy, Datasheet. 2006.
  22. Vattappara K, Hosseini VA, Joseph C, Hanning F, Andersson J. Physical and thermodynamic simulations of gamma-prime precipitation in Haynes® 282® using arc heat treatment. *J Alloys Compd.* 2021;870:159484. <https://doi.org/10.1016/j.jallcom.2021.159484>.
  23. Polkowska A, et al. Microstructure and hardness evolution in Haynes 282 Nickel-based superalloy during multi-variant aging heat treatment. *J Mater Eng Perform.* 2019;28(7):3844–51. <https://doi.org/10.1007/s11665-019-3886-0>.
  24. Shaikh AS, Schulz F, Minet-Lallemend K, Hryha E. Microstructure and mechanical properties of Haynes 282 superalloy produced by laser powder bed fusion. *Mater Today Commun.* 2021;26(January):102038. <https://doi.org/10.1016/j.mtcomm.2021.102038>.
  25. Otto R, et al. Roadmap for additive manufacturing of HAYNES® 282® superalloy by laser beam powder bed fusion (PBF-LB) technology. *Mater Des.* 2021;204:109656. <https://doi.org/10.1016/j.matdes.2021.109656>.
  26. Yang Y. Microstructural evolution of large cast haynes 282 at elevated temperature. *Crystals (Basel).* 2021. <https://doi.org/10.3390/cryst11080867>.
  27. Deshpande A, Nath SD, Atre S, Hsu K. Effect of post processing heat treatment routes on microstructure and mechanical property evolution of Haynes 282 Ni-based superalloy fabricated with selective laser melting (SLM). *Metals (Basel).* 2020;10(5):1–13. <https://doi.org/10.3390/met10050629>.
  28. Kirka MM, Unocic KA, Kruger K, Forsythe A. Process development for Haynes® 282® using additive manufacturing. Oak Ridge, TN (United States). 2018. <https://doi.org/10.2172/1435227>.
  29. Unocic KA, Kirka MM, Cakmak E, Greeley D, Okello AO, Dryepondt S. Evaluation of additive electron beam melting of Haynes 282 alloy. *Mater Sci Eng A.* 2020;772(June 2019):138607. <https://doi.org/10.1016/j.msea.2019.138607>.
  30. Amperprint® 0233 Haynes® 282® Advanced nickel superalloy for powder bed fusion-General material description. 2020. <https://www.hogans.com/am> (Online).
  31. Molak RM, Paradowski K, Brynk T, Ciupinski L, Pakiela Z, Kurzydowski KJ. Measurement of mechanical properties in a 316L stainless steel welded joint. *Int J Press Vessels Pip.* 2009;86(1):43–7. <https://doi.org/10.1016/j.ijpvp.2008.11.002>.
  32. Brynk T, et al. Fatigue crack growth rate and tensile strength of Re modified Inconel 718 produced by means of selective laser melting. *Mater Sci Eng A.* 2017;698(October 2016):289–301. <https://doi.org/10.1016/j.msea.2017.05.052>.
  33. Pike LM. Development of a fabricable gamma-prime ( $\gamma'$ ) strengthened superalloy. In: *Proceedings of the International Symposium on Superalloys.* 2008. pp. 191–200.
  34. Christofidou KA, et al. Microstructural Control and Optimization of Haynes 282 Manufactured Through Laser Powder Bed Fusion. *Miner Metals Mater Ser.* 2020. [https://doi.org/10.1007/978-3-030-51834-9\\_99](https://doi.org/10.1007/978-3-030-51834-9_99).
  35. Gao Y, Ding Y, Chen J, Xu J, Ma Y, Wang X. Effect of twin boundaries on the microstructure and mechanical properties of Inconel 625 alloy. *Mater Sci Eng A.* 2019;767(August):138361. <https://doi.org/10.1016/j.msea.2019.138361>.
  36. Pike LM. Long term thermal exposure of Haynes 282 alloy. In: *7th International Symposium on Superalloy 718 and Derivatives 2010*, vol. 2. 2010. pp. 645–660. [https://doi.org/10.7449/2010/superalloys\\_2010\\_645\\_660](https://doi.org/10.7449/2010/superalloys_2010_645_660).
  37. Pavan AHV, Narayan RL, Li SH, Singh K, Ramamurty U. Mechanical behavior and dynamic strain ageing in Haynes®282 superalloy subjected to accelerated ageing. *Mater Sci Eng A.* 2022. <https://doi.org/10.1016/j.msea.2021.142486>.
  38. Unocic KA, Kirka MM, Cakmak E, Greeley D, Okello AO, Dryepondt S. Evaluation of additive electron beam melting of haynes 282 alloy. *Mater Sci Eng A.* 2020. <https://doi.org/10.1016/j.msea.2019.138607>.
  39. Ghiaasiaan R, Ahmad N, Gradl PR, Shao S, Shamsaei N. Additively manufactured Haynes 282: effect of unimodal vs. bimodal  $\gamma'$ - microstructure on mechanical properties. *Mater Sci Eng A.* 2022. <https://doi.org/10.1016/j.msea.2021.142234>.
  40. HAYNES® 282® alloy Principal Features. 2021.
  41. Shaikh AS, Schulz F, Minet-Lallemend K, Hryha E. Microstructure and mechanical properties of Haynes 282 superalloy produced by laser powder bed fusion. *Mater Today Commun.* 2021. <https://doi.org/10.1016/j.mtcomm.2021.102038>.
  42. Harrison NJ, Todd I, Mumtaz K. Reduction of micro-cracking in nickel superalloys processed by selective laser melting: a fundamental alloy design approach. *Acta Mater.* 2015;94:59–68. <https://doi.org/10.1016/j.actamat.2015.04.035>.

**Publisher's Note** Springer Nature remains neutral with regard to jurisdictional claims in published maps and institutional affiliations.